

More relaxed intracluster gas than galaxies in clusters in quasi-equilibrium

Z. S. Yuan,^{1,2} * J. L. Han,^{1,2,3} † H. Böhringer,^{4,5} Z. L. Wen,^{1,2} and G. Chon⁴

1. National Astronomical Observatories, Chinese Academy of Sciences, 20A Datun Road, Chaoyang District, Beijing 100101, China

2. CAS Key Laboratory of FAST, NAOC, Chinese Academy of Sciences, Beijing 100101, China

3. School of Astronomy, University of Chinese Academy of Sciences, Beijing 100049, China

4. University Observatory, Ludwig-Maximilians-Universität München, Scheinerstr. 1, 81679 München, Germany

5. Max-Planck-Institut für Extraterrestrische Physik, 85748 Garching, Germany

Accepted XXX. Received YYY; in original form ZZZ

ABSTRACT

During cluster mergers, the intracluster gas and member galaxies undergo dynamic evolution, but at different timescales and reach different states. We collect 24 galaxy clusters in quasi-equilibrium state as indicated by the X-ray image, and calculate the cluster orientations and three kinds of dynamical parameters, i.e., the normalized centroid offset, the sphere index and the ellipticity, for these clusters from the distributions of member galaxies and also the intracluster gas. We find consistent alignments for the orientations estimated from the two components. However, the three kinds of dynamical parameters indicated by member galaxies are systematically larger than those derived from the gas component, suggesting that the gas component is more relaxed than member galaxies. Differences of dynamical features between the intracluster gas and member galaxies are independent of cluster mass and concentration. We conclude that the intracluster gas reaches the dynamic equilibrium state earlier than the almost collisionless member galaxies.

Key words: galaxies: clusters: general — galaxies: clusters: intracluster medium

1 INTRODUCTION

Galaxy clusters have been idealized to have spherically symmetric structures in many studies, such as those on cluster mass estimation (e.g., Arnaud et al. 2010; Piffaretti et al. 2011). Observations, however, indicate that most clusters of galaxies have elliptical or irregular morphologies (e.g., Mann & Ebeling 2012). In the hierarchical structure formation scenario, galaxy clusters grow through mergers of smaller subclusters or groups and the accretion of material (e.g., Berrier et al. 2009; McGee et al. 2009). In the early stage of merging, violent dynamic interactions occur between subclusters, matter in the cluster is generally stretched along the merging axis, the cluster therefore shows a bimodal or elongated morphology (e.g., Roettiger et al. 1993, 1996, 1997). After the fast and violent merging stage, matter in the cluster roughly follows a 3-dimensional Gaussian distribution and the cluster shows an elliptical morphology (e.g., Lynden-Bell 1967). After evolving further for several Giga-years, the merged clusters will approach a state of virial and hydrostatic equilibrium, and have almost spherically symmetric structures (see simulations, e.g., Poole et al. 2006).

During cluster merging, the intracluster medium (ICM) evolves differently from the member galaxies and dark matter

mainly because the former is viscous while the latter are almost collisionless. Observationally, the Bullet cluster (1E 0657–56, e.g., Markevitch et al. 2002) is a textbook example: the distribution of the ICM shows a large discrepancy to that of member galaxies and dark matter (Clowe et al. 2004, 2006). Simulations have shown that the dark matter of merging clusters generally exhibits a more elongated morphology (McDonald et al. 2022) and requires a longer time to reach the equilibrium state than the ICM (see figure 15 and 16 in Poole et al. 2006). After reaching the virilization state, relaxed clusters recover a good spatial matching between the ICM, member galaxies and dark matter (e.g., Clowe & Schneider 2002; Donnarumma et al. 2011). Due to continuous radiative cooling of ICM, relaxed clusters are often highly concentrated in X-ray with a very bright cool-core in the cluster center (see Fabian 2012, as a review).

Many efforts have been made to quantify the dynamical state of galaxy clusters with optical or X-ray data (e.g., Ramella et al. 2007; Santos et al. 2008; Wen & Han 2013; Yuan et al. 2022). The ellipticity has been widely used to describe the global morphology of galaxy clusters. In the optical, the cluster ellipticity can be estimated from the projected distribution of member galaxies (e.g., Carter & Metcalfe 1980; de Theije et al. 1995; Splinter et al. 1997). In X-rays, one can directly obtain the cluster ellipticity by fitting the brightness image with a two-dimensional β -model (e.g., Yuan & Han 2020; Yuan & Wen 2022). Buote & Canizares

* E-mail: zsyuan@nao.cas.cn

† E-mail: hjl@nao.cas.cn

(1992) studied five Abell clusters and found that the ellipticities derived from the ICM are smaller than those calculated by Carter & Metcalfe (1980) with member galaxies. Struble & Ftaclas (1994) reported that more massive clusters tend to have a rounder morphology. The cluster ellipticity has weak or no redshift evolution (e.g., Plionis 2002).

Theories and simulations predict that the dynamic relaxation for the almost-collisionless dark matter and member galaxies differs from that of the diffuse ICM (e.g., Poole et al. 2006). Observational differences between member galaxies and ICM have been established in clusters in early stages of merging, such as in the Bullet cluster. However, does this difference persist in clusters in later stages of dynamic evolution? In this work, we report on systematic differences in dynamic features between the distributions of member galaxies in the optical band and the ICM expressed by the X-ray image. Recently, we processed the X-ray images homogeneously for 1844 clusters with the archival data of the *Chandra* and *XMM-Newton* satellites (Yuan & Han 2020; Yuan et al. 2022), and therefore have a dataset available. In optical, a large number of clusters have been identified with well-recognized member galaxies (e.g., Wen et al. 2012; Wen & Han 2015). Therefore, it is now feasible to study the distributions of member galaxies and the ICM for a large sample of clusters. The distributions of the two components could be very complex and vary among galaxy clusters in different dynamical states. As the first step, in this paper we compare the dynamic features of member galaxies and ICM only for clusters in a quasi-equilibrium state.

The paper is structured as follows. In Section 2, we describe the methods we used to select the cluster sample and derive the parameters. In Section 3, we discuss the dynamic features of member galaxies and ICM. A brief summary is given in Section 4. Throughout this paper, a flat Λ CDM cosmology is adopted with $H_0 = 70$ km s $^{-1}$ Mpc $^{-1}$, $\Omega_m = 0.3$ and $\Omega_\Lambda = 0.7$.

2 CLUSTER SAMPLE AND PARAMETERS

By processing the archival data of the *Chandra* and *XMM-Newton* satellites, we obtained X-ray images for 1844 galaxy clusters and calculated four kinds of dynamical parameters for them (Yuan & Han 2020; Yuan et al. 2022). The clusters are collected from both targeted and serendipitous observations. The data of the two satellites are processed with similar strategies: only photons in 0.5–5 keV are used; the point sources are carefully identified and replaced by the brightness of their ambient regions; the images are exposure corrected and background subtracted; the X-ray images are smoothed to a physical scale of 30 kpc to avoid an observational bias that the pixel size indicates different physical scale for clusters at different redshifts. Detailed information on data processing can be found in the Section 2 of Yuan & Han (2020) and Yuan et al. (2022).

The optical data for member galaxies of clusters are taken from the *Sloan Digital Sky Survey* (SDSS) following Wen & Han (2015). Galaxies are recognized as cluster members when their r -band evolution-corrected absolute magnitude M_r^c are brighter than -20.0 mag and their velocity differences from the cluster are less than 2500 km s $^{-1}$ if spectroscopic redshifts are available or the redshift differences are less than $0.04(1+z)$ if only photometric redshifts are available (Wen & Han 2015). Wen et al. (2009) showed that using only photometric redshifts yields a completeness about 90% and a contamination rate of about 20% for member galaxies when $z < 0.42$.

We select a sample of galaxy clusters for this work with the following four criteria. (1) The cluster is in quasi-equilibrium when $\log_{10}(c) > -0.5$, where c is the concentration index. Here we use the concentration index c instead of the morphology index δ because the latter is defined from the cluster ellipticity (Yuan & Han 2020). (2) The X-ray image of the cluster has a good quality within $0.5r_{500}$, i.e., the region encircled by $0.5r_{500}$ is well covered by the 3σ contour of the X-ray image. Here r_{500} is the radius in which the mean matter density of the cluster is 500 times of the local critical density. (3) The cluster redshift should be lower than 0.3 to ensure that member galaxies with r -band absolute magnitude brighter than -20.0 mag are highly complete ($> 90\%$). We visually checked the optical images of these clusters to avoid contamination of foreground stars. (4) The number of satellite galaxies in $0.5r_{500}$, N_{sat} , is larger than 20 to ensure that the calculated parameters are reliable. Finally, we get 24 clusters satisfying all the above criteria, see Table 1. The X-ray images with superimposed distribution of member galaxies for the 24 clusters are shown in Fig. 1.

We collect various parameters of the clusters from literature. The coordinate and redshift of the BCG measured from the SDSS data, see Wen et al. (2012) for details, are regarded as that of their host clusters. Clusters with $z < 0.05$ are not contained in the catalogue of Wen & Han (2015), we thus identify the BCG and other member galaxies with the same method for A2052 ($z = 0.0345$), A2063 ($z = 0.0341$) and A2199 ($z = 0.0312$). The concentration indices c are taken from Yuan et al. (2022). The cluster radius r_{500} and mass M_{500} come from the catalogue compiled by Piffaretti et al. (2011).

Virialized galaxy clusters generally show a small offset between the brightness peak and the flux-weighted centroid, but the offset could be large for disturbed clusters. We define a vector named the normalized centroid offset $\vec{\eta}$ as

$$\vec{\eta} = \frac{\vec{\mu}_{10} + \vec{\mu}_{01}}{r_{500}}, \quad (1)$$

where

$$\vec{\mu}_{10} = \frac{1}{\sum_i f_{w,i}} \sum_i f_{w,i} \cdot \vec{x}_i, \quad \vec{\mu}_{01} = \frac{1}{\sum_i f_{w,i}} \sum_i f_{w,i} \cdot \vec{y}_i. \quad (2)$$

The $f_{w,i}$ denotes the weighted brightness for the hot gas or member galaxies at the i th pixel, here (\vec{x}_i, \vec{y}_i) is the relative coordinate of the i th pixel to the cluster center. For the 24 quasi-equilibrium clusters in our sample, we separately take the X-ray brightness peak as the center for the ICM and the position of BCG as the center for member galaxies, though the deviations between the X-ray peak and the BCG are small for these quasi-equilibrium clusters, see Fig. 1. Briefly speaking, the $\vec{\eta}_{\text{gal}}$ for member galaxies indicates the normalized offset between the BCG and the optical flux-weighted centroid, while the $\vec{\eta}_{\text{ICM}}$ means the departure from the X-ray brightness peak to the X-ray flux-weighted centroid.

The dynamical state of member galaxies and hot gas could be compared with the derived mass distribution, rather than their brightness distribution. In optical, the mass of galaxies is approximately proportional to their luminosity (e.g., Faber & Jackson 1976). In X-ray, the brightness of hot gas is broadly proportional to the square of the in-situ mass (e.g., Piffaretti & Valdarnini 2008). We calculate the dynamical parameters using the weighted brightness $f_{w,i}$, which is defined as

$$\begin{cases} f_{w,i} = \sqrt{f_i} & (\text{for ICM}), \\ f_{w,i} = f_i & (\text{for galaxy}), \end{cases} \quad (3)$$

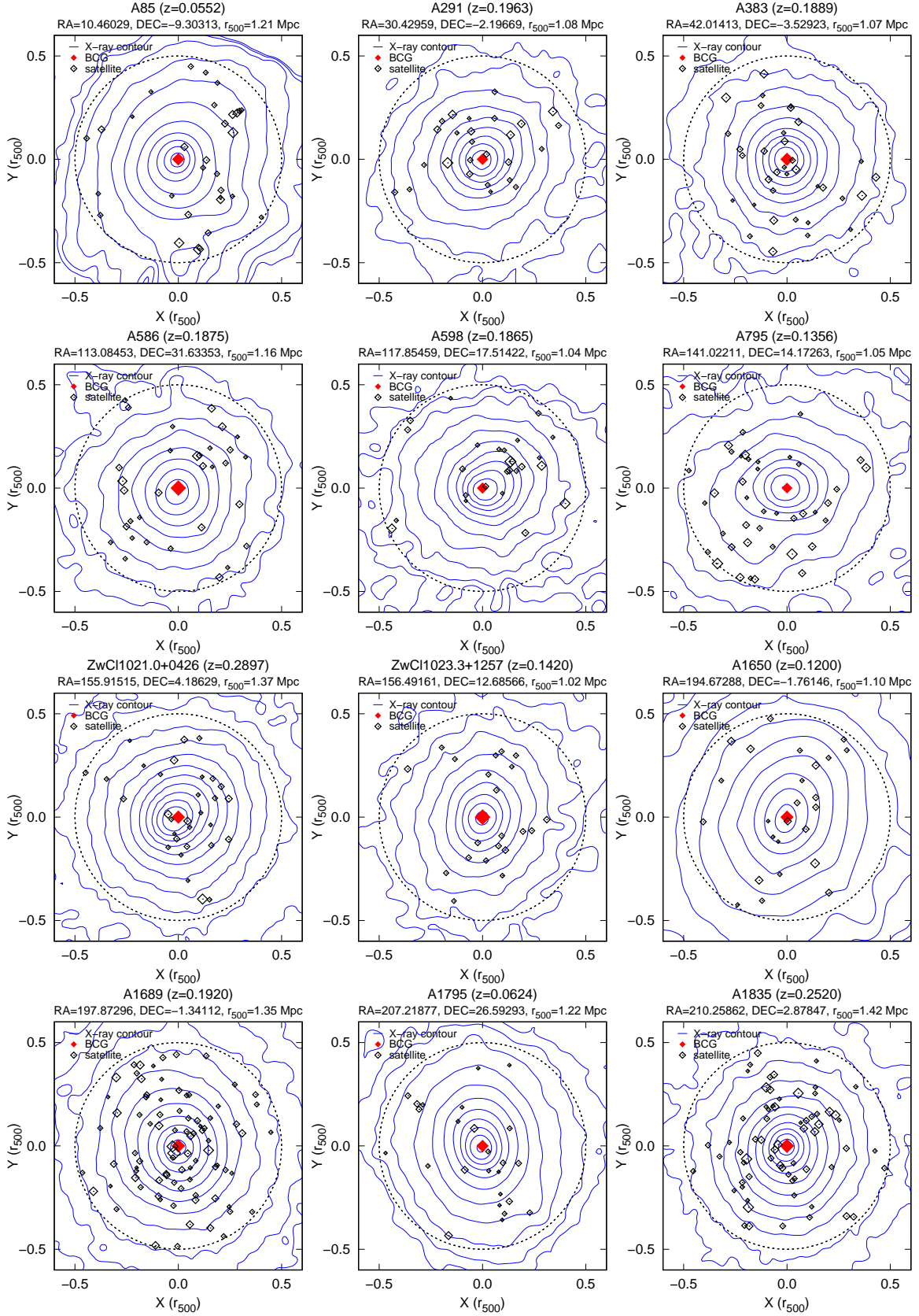


Figure 1. - continued

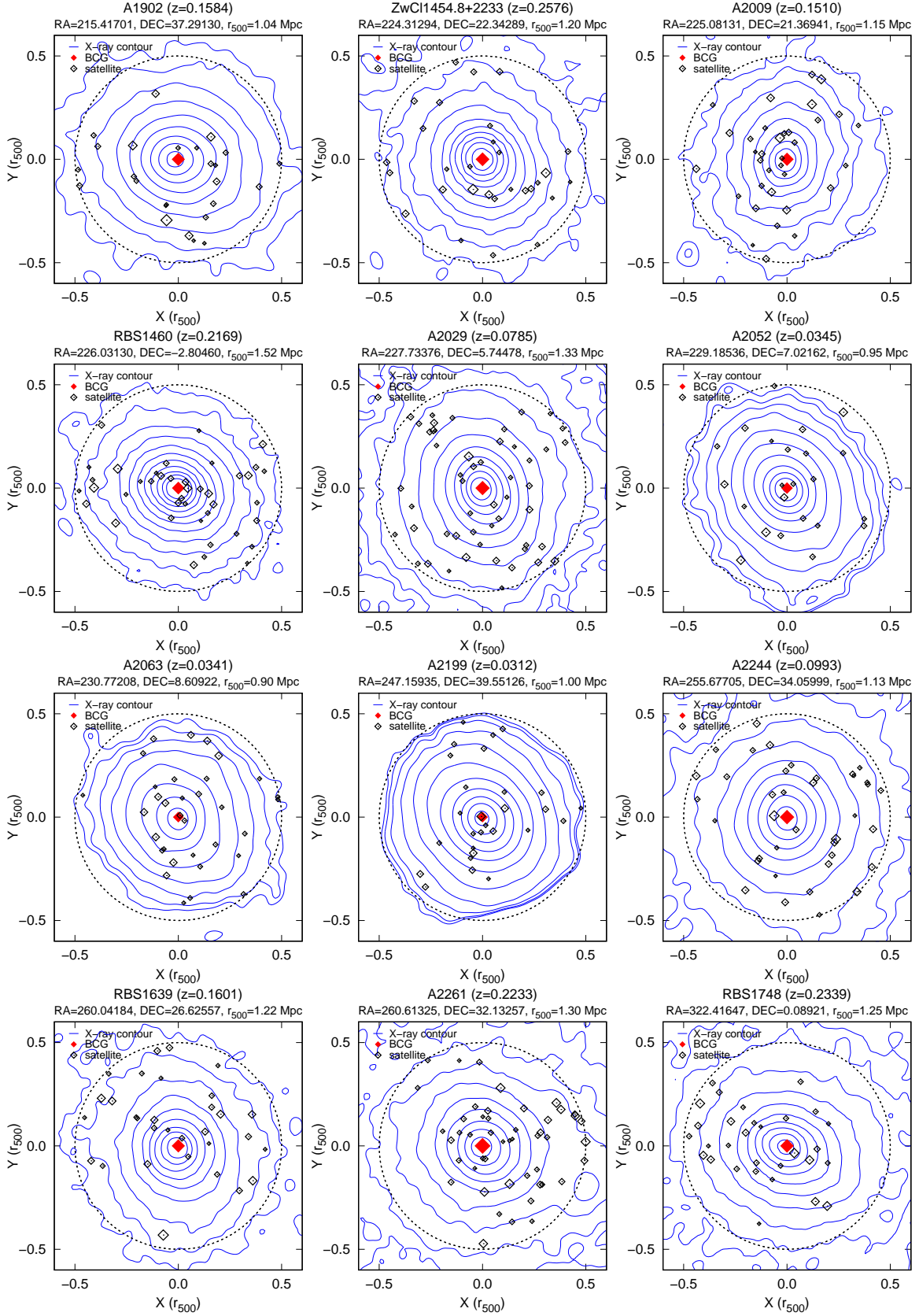


Figure 1. X-ray images with superimposed member galaxies for the 24 clusters. The X-axis and Y-axis of each image are scaled with r_{500} . The coordinate, redshift and physical scale of r_{500} for each cluster are written on the top of each panel. Contours indicate the distribution of X-ray brightness, at levels of $\langle S_{bg} \rangle + 3 \times 2^n \sigma \text{ cnt s}^{-1} \text{ deg}^{-2}$. Here $\langle S_{bg} \rangle$ and σ are the mean and fluctuation of the background, which are calculated in a clean region around the cluster, and $n = 0, 1, 2, \dots$. The solid and open diamonds denote the BCG and satellite galaxies respectively, and their sizes correspond to the luminosity of the galaxy. The large dotted circle shows the radius of $0.5r_{500}$, within which both the optical and X-ray parameters are calculated.

Table 1. Parameters for the 24 clusters in quasi-equilibrium state.

Name	RA (J2000)	DEC (J2000)	z	$\log_{10}(c)$	r_{500} (Mpc)	M_{500} ($10^{14} M_{\odot}$)	N_{sat}	$\vec{\eta}_{\text{ICM}}$		γ_{ICM} (%)	e_{ICM}	ϕ_{ICM} ($^{\circ}$)	$\vec{\eta}_{\text{gal}}$		γ_{gal} (%)	e_{gal}	ϕ_{gal} ($^{\circ}$)
								(X-axis, %)	(Y-axis, %)				(X-axis, %)	(Y-axis, %)			
(1)	(2)	(3)	(4)	(5)	(6)	(7)	(8)	(9)	(10)	(11)	(12)	(13)	(14)	(15)	(16)	(17)	(18)
A85	10.46029	-9.30313	0.0552	-0.42±0.01	1.21	5.32	31	0.72±0.20	-1.36±0.23	29.3±8.0	0.07±0.01	170.7±0.3	10.26±4.24	-5.38±6.97	48.3±7.7	0.21±0.01	174.3±5.9
A291	30.42959	-2.19669	0.1963	-0.31±0.01	1.08	4.31	26	-0.33±0.20	0.09±0.20	26.3±7.4	0.03±0.01	140.3±0.3	-1.17±4.91	7.38±3.00	45.2±5.9	0.37±0.01	112.8±0.4
A383	42.01413	-3.52923	0.1889	-0.29±0.01	1.07	4.25	35	1.10±0.19	-0.16±0.20	26.5±8.4	0.01±0.01	13.4±1.1	0.65±4.62	-2.22±5.08	43.2±9.0	0.34±0.06	33.2±0.6
A586	113.08453	31.63353	0.1875	-0.49±0.02	1.16	5.20	32	0.74±0.21	0.67±0.21	24.5±6.6	0.02±0.01	131.7±0.3	0.28±4.41	2.61±4.43	33.1±4.5	0.12±0.01	153.2±2.3
A598	117.85459	17.51422	0.1865	-0.30±0.01	1.04	3.82	26	1.12±0.20	1.91±0.19	25.4±5.4	0.03±0.01	103.6±0.1	8.40±7.57	6.63±3.70	36.6±5.6	0.39±0.01	99.7±0.3
A795	141.02211	14.17263	0.1356	-0.42±0.01	1.05	3.81	40	0.59±0.23	-1.12±0.21	27.2±8.2	0.07±0.01	113.2±0.1	-9.89±4.86	-13.24±5.59	60.7±7.0	0.30±0.01	141.6±0.8
ZwCl1021.0+0426	155.91515	4.18629	0.2897	-0.29±0.01	1.37	9.17	31	1.79±0.18	1.40±0.19	24.4±4.8	0.03±0.01	146.0±0.3	3.79±3.07	-0.39±6.65	44.1±5.8	0.41±0.05	19.0±0.6
ZwCl1023.3+1257	156.49161	12.68566	0.1420	-0.37±0.01	1.02	3.48	21	0.06±0.20	1.03±0.22	25.3±5.6	0.06±0.01	158.0±0.2	3.21±4.11	1.08±4.58	42.2±8.2	0.23±0.03	12.9±1.7
A1650	194.67288	-1.76146	0.1200	-0.44±0.01	1.10	4.12	25	0.81±0.21	1.40±0.23	24.1±5.1	0.06±0.01	159.8±0.2	-0.28±4.01	3.63±6.09	47.3±9.2	0.33±0.02	5.4±1.0
A1689	197.87296	-1.34112	0.1920	-0.43±0.01	1.35	8.39	85	-0.40±0.19	1.42±0.20	28.1±6.6	0.04±0.01	14.6±0.2	-2.43±2.13	-0.21±2.52	34.6±6.4	0.21±0.02	15.7±0.4
A1795	207.21877	26.59293	0.0624	-0.32±0.01	1.22	5.53	25	0.53±0.19	1.20±0.21	26.8±6.8	0.06±0.01	15.2±0.1	-5.91±4.03	-5.66±5.65	49.6±6.8	0.30±0.05	26.9±0.4
A1835	210.25862	2.87847	0.2520	-0.30±0.01	1.42	10.50	66	0.43±0.18	0.02±0.19	25.9±7.6	0.03±0.01	168.8±0.5	-1.54±2.59	1.83±3.40	33.5±4.7	0.21±0.01	164.0±1.5
A1902	215.41701	37.29130	0.1584	-0.39±0.01	1.04	3.80	25	2.54±0.21	0.15±0.20	28.9±8.7	0.05±0.01	67.7±0.1	-2.62±4.38	-10.12±7.15	50.7±5.7	0.07±0.02	49.8±1.1
ZwCl1454.8+2233	224.31294	22.34289	0.2576	-0.26±0.01	1.20	6.32	29	0.02±0.18	-0.39±0.19	27.0±8.6	0.04±0.01	27.0±0.3	-2.52±3.13	4.53±5.01	35.3±9.0	0.15±0.02	59.6±0.8
A2009	225.08131	21.36941	0.1510	-0.38±0.01	1.15	5.06	34	0.58±0.20	0.14±0.22	26.3±7.2	0.05±0.01	163.1±0.3	-0.89±5.30	-1.93±2.39	42.3±6.2	0.37±0.01	158.8±0.9
RBS1460	226.03130	-2.80461	0.2169	-0.21±0.01	1.52	12.48	41	-0.52±0.18	-0.33±0.17	27.6±8.0	0.05±0.01	58.8±0.1	-0.90±3.35	-3.44±4.09	45.6±7.3	0.47±0.02	85.4±0.1
A2029	227.73376	5.74478	0.0785	-0.35±0.01	1.33	7.27	51	0.68±0.19	-0.63±0.21	28.1±8.9	0.05±0.01	11.7±0.2	-0.07±4.95	0.28±6.47	45.1±9.6	0.21±0.02	22.5±0.8
A2052	229.18536	7.02162	0.0345	-0.28±0.01	0.95	2.49	23	-0.10±0.21	-0.68±0.22	27.6±8.6	0.05±0.01	33.1±0.2	3.85±2.87	3.48±4.48	36.0±6.0	0.27±0.01	156.1±1.7
A2063	230.77208	8.60922	0.0341	-0.46±0.01	0.90	2.16	33	-0.16±0.23	0.97±0.23	27.0±7.5	0.02±0.01	44.2±0.4	0.76±3.33	-0.21±4.07	37.6±4.2	0.23±0.01	172.5±2.7
A2199	247.15935	39.55126	0.0312	-0.31±0.01	1.00	2.96	28	-0.41±0.20	0.72±0.21	27.7±7.6	0.04±0.01	34.5±0.3	5.70±4.31	-0.99±4.16	40.4±6.4	0.31±0.01	152.0±0.7
A2244	255.67705	34.05999	0.0993	-0.45±0.01	1.13	4.49	38	0.23±0.20	-0.37±0.21	26.4±8.1	0.02±0.01	170.5±0.6	8.35±4.26	-8.69±4.01	40.1±8.8	0.26±0.04	49.5±0.5
RBS1639	260.04184	26.62557	0.1604	-0.30±0.01	1.22	6.01	31	-0.09±0.19	-0.04±0.21	26.4±8.1	0.05±0.01	17.8±0.2	-1.21±5.12	4.01±6.63	37.8±7.5	0.15±0.03	40.9±0.7
A2261	260.61325	32.13257	0.2233	-0.43±0.01	1.30	7.88	48	1.43±0.21	-0.27±0.20	27.7±9.2	0.04±0.01	75.5±0.1	17.16±4.46	1.08±3.74	51.7±7.0	0.26±0.02	98.9±0.2
RBS1748	322.41647	0.08921	0.2339	-0.36±0.01	1.25	7.04	30	1.64±0.21	-0.67±0.19	29.4±9.7	0.06±0.01	69.0±0.1	-12.57±5.40	-0.29±3.72	67.1±11.5	0.49±0.05	68.1±0.2

Notes: Columns: (1) cluster name; (2 - 4) right ascension, declination and redshift of the BCG measured from the SDSS data; (5) the concentration index of the cluster, taken from Yuan et al. (2022); (6 - 7) the radius and mass of the cluster, from Piffaretti et al. (2011); (8) the number of member galaxies brighter than -20.0 mag in $0.5r_{500}$; (9 - 10) the normalized offset between the brightness peak and the estimated centroid from the cluster X-ray image, values in the X-axis and Y-axis are presented separately; (11 - 13) the sphere index, the ellipticity and the position angle calculated from the X-ray image; (14 - 15) the normalized offset between the BCG and the centroid estimated from member galaxies in X-axis and Y-axis; (16 - 18) the sphere index, the ellipticity and position angle estimated from the distribution of member galaxies.

where f_i is the pixel value of X-ray images or the luminosity of member galaxies.

Ideally, a relaxed galaxy cluster shows a spherically symmetric morphology, thus the radial profiles of the matter distribution should be similar in any directions. We define the sphere index γ to quantify the degree of spherical symmetry of the ICM and member galaxies in clusters. First, we define a frame from the cluster center with an arbitrary position angle θ , and the two perpendicular axes of the frame divide the image into four quadrants. Second, we calculate the parameter $S_{\theta,n}$ as the sum of all pixels in the n th quadrant as

$$S_{\theta,n} = \sum_i f_{w,i} \cdot r_i, \quad (4)$$

the r_i is the distance from the i th pixel to the cluster center, and $n = 1, 2, 3, 4$. Then, the ΔS_{θ} is defined as

$$\Delta S_{\theta} = S_{\theta,\max} - S_{\theta,\min}, \quad (5)$$

where $S_{\theta,\max}$ ($S_{\theta,\min}$) is the maximum (minimum) among the ($S_{\theta,1}, S_{\theta,2}, S_{\theta,3}, S_{\theta,4}$). Last, we search for the θ , that yields a maximum value for ΔS_{θ} , and the sphere index γ is defined as

$$\gamma = \frac{\max(\Delta S_{\theta})}{S_{\text{tot}}} = \frac{\max(\Delta S_{\theta})}{\sum_{n=1}^4 S_{\theta,n}} \times 100\%. \quad (6)$$

In short, the γ indicates the largest difference in matter distribution between any two quadrants. More relaxed clusters are expected to have a smaller γ .

The ellipticity and orientation of galaxy clusters has been calculated with different methods (e.g., [Carter & Metcalfe 1980](#); [Niederste-Ostholt et al. 2010](#); [Huang et al. 2016](#); [Yuan & Wen 2022](#)). To avoid a possible bias caused by different methods, here cluster ellipticities and orientations from optical and X-ray data are calculated in the same way. We choose the moments method, which has been widely used for optical data, but adopt the new weight of brightness $f_{w,i}$ rather than the traditional weight of $\frac{1}{r_i^2}$ (e.g., [Niederste-Ostholt et al. 2010](#); [Huang et al. 2016](#)) to make the method also applicable to diffuse X-ray images. The second-order moments are defined as

$$\begin{aligned} \mu_{20} &= \frac{1}{\sum_i f_{w,i}} \sum_i f_{w,i} \cdot x_i^2, \\ \mu_{02} &= \frac{1}{\sum_i f_{w,i}} \sum_i f_{w,i} \cdot y_i^2, \\ \mu_{11} &= \frac{1}{\sum_i f_{w,i}} \sum_i f_{w,i} \cdot x_i y_i. \end{aligned} \quad (7)$$

The major and minor axes of the cluster, Λ_a and Λ_b , can be computed through the following equation (e.g., [Carter & Metcalfe 1980](#))

$$\begin{vmatrix} \mu_{20} - \Lambda^2 & \mu_{11} \\ \mu_{11} & \mu_{02} - \Lambda^2 \end{vmatrix} = 0. \quad (8)$$

The cluster ellipticity is defined as

$$e = 1 - \frac{\Lambda_b}{\Lambda_a}. \quad (9)$$

The position angle of the cluster is calculated with

$$\phi = \arctan\left(\frac{\mu_{02} - \Lambda_a^2}{\mu_{11}}\right), \quad (10)$$

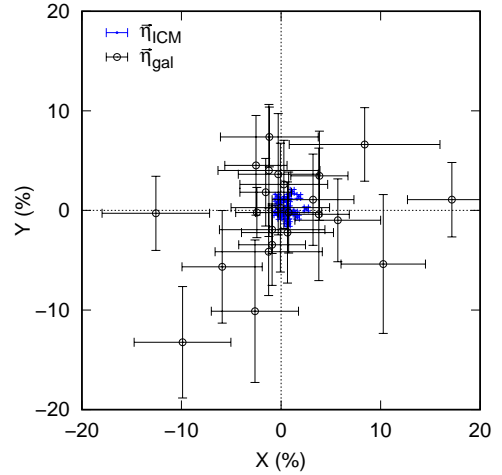


Figure 2. The distribution of the normalized centroid offsets estimated from the ICM (\bar{n}_{ICM}) and member galaxies (\bar{n}_{gal}). The intersection of the dotted lines indicate the position of the X-ray brightness peak for \bar{n}_{ICM} and the position of BCG for \bar{n}_{gal} . The errorbars of each point are the Poisson errors.

here the ϕ is from the north through the east. The deviation between position angles measured from the distributions of member galaxies (ϕ_{gal}) and ICM (ϕ_{ICM}) is denoted as

$$\begin{cases} \Delta\phi = |\phi_{\text{gal}} - \phi_{\text{ICM}}| & (|\phi_{\text{gal}} - \phi_{\text{ICM}}| \leq 90^\circ), \\ \Delta\phi = 180^\circ - |\phi_{\text{gal}} - \phi_{\text{ICM}}| & (|\phi_{\text{gal}} - \phi_{\text{ICM}}| > 90^\circ). \end{cases} \quad (11)$$

Here $\Delta\phi$ is in the range of $0^\circ \leq \Delta\phi \leq 90^\circ$.

Considering the possible ellipticity changes at different cluster radii (e.g., [Splinter et al. 1997](#)) and also biases for other parameters, we calculate the normalized centroid offsets, sphere indices, ellipticities and position angles from optical and X-ray images in the same region encircled by $0.5r_{500}$, see the large dotted circles in Fig. 1.

3 DIFFERENT RELAXED STATE FOR MEMBER GALAXIES AND ICM

The exact dynamical state should be derived from the 3 dimensional velocities of all kinds of matter in a cluster. However, the velocities of dark matter and intracluster gas are not available. For galaxies, only the velocity along the line of sight can be well measured by the spectroscopic redshifts, which are available only for a small fraction of members. Therefore, in this paper, we only consider the mass distribution in the sky plane for the intracluster gas and member galaxies. Clear displacements between the ICM and member galaxies have been observed in many merging clusters (e.g., [Maugorato et al. 2008](#); [Dawson et al. 2012](#); [Jee et al. 2014](#); [Golovich et al. 2016, 2017](#)), as member galaxies, similar to the dark matter, move almost collisionless during the cluster merger, while the intracluster gas evolves under dynamic pressures (e.g., [Powell et al. 2009](#)). The simulation made by [Poole et al. \(2006\)](#) indicates that the dark matter generally takes longer time to reach the virialization state than the gaseous component, especially for mergers between subclusters with large mass difference (e.g., $m_1 : m_2 < 1 : 3$). Considering that both member galaxies and the dark matter are almost collisionless, it is natural to expect the relaxation time for member galaxies is also longer than that of the ICM. In the following, we show the different relaxed state of member galaxies and ICM in the 24 quasi-equilibrium clusters.

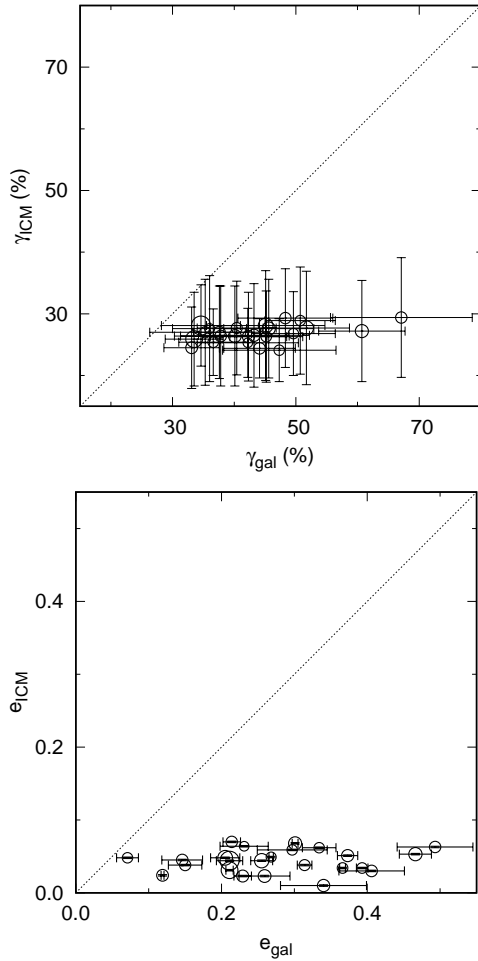


Figure 3. Comparisons of the sphere indices (upper panel) and ellipticities (lower panel) of clusters measured from member galaxies and ICM. The circle size is proportional to $\sqrt{N_{\text{sat}}}$. The dotted lines in both panels show the equivalence for the X-axis and Y-axis. The errorbars in the two panels are the Poisson errors.

The departure of the flux-weighted centroid from the brightness peak is generally very small for symmetric distributions, but could be large for disturbed systems. In Fig. 2, the distribution of normalized centroid offsets is shown for the ICM ($\vec{\eta}_{\text{ICM}}$, dots) and member galaxies ($\vec{\eta}_{\text{gal}}$, circles). It is clear that the offsets calculated from member galaxies ($\langle \vec{\eta}_{\text{gal}} \rangle = 6.11\% r_{500}$) are more scattered than those from the ICM ($\langle \vec{\eta}_{\text{ICM}} \rangle = 1.12\% r_{500}$).

Observationally, galaxy clusters in dynamical equilibrium state usually show a roundish morphology with a small difference in any direction. In Fig. 3, we compare the sphere indices (upper panel) and ellipticities (lower panel) of clusters measured from distributions of member galaxies and ICM. The upper panel shows that all the 24 clusters exhibit larger non-spherical symmetry for member galaxies than for the ICM. The lower panel indicates that all clusters show larger e_{gal} , suggesting that the distribution of member galaxies is more elongated than that of the diffuse ICM. If we take galaxies as the tracer of dark matter, our result is consistent with the simulations made by McDonald et al. (2022), which show that $\sim 90\%$ clusters display a more elongated dark matter morphology when compared to the gaseous component.

In Fig. 4, we show the distribution of $\Delta\phi$, the deviation angle between cluster orientations estimated from member galaxies and the ICM, for the 24 clusters. It is clear that the cluster ori-

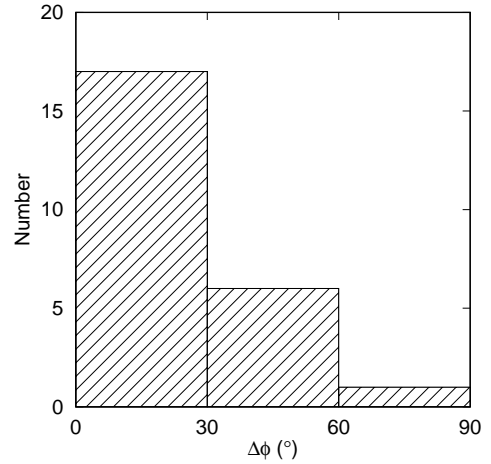


Figure 4. The distribution of $\Delta\phi$ for the 24 clusters, $\Delta\phi$ is the difference between cluster orientations estimated from member galaxies and the ICM.

entations indicated by member galaxies tend to align with those measured from the ICM, which is consistent with our recent work (Yuan & Wen 2022). The orientation uncertainties are generally very small, see Table 1, so the alignment will not be significantly weakened by data uncertainties. The spatial orientation is the reflection of cluster angular momentum, which is further linked to the direction(s) of the post merger(s). The orientation alignment shown in Fig. 4 indicates that the information of post mergers is stored simultaneously in the distributions of member galaxies and ICM, though the structures of the two components differ in detail.

The large discrepancy between the ICM and member galaxies in clusters, like in the Bullet cluster, indicates that they evolve differently in the early stages of merging. The results presented in this paper describe the picture of dynamic evolution in later stages. The angular momentum accompanied by the post-merger is stored in or transformed into the ICM and member galaxies simultaneously, therefore the cluster orientations indicated by the two matter components are consistent with each other. The diffuse ICM evolves under non-negligible viscosity, causing the angular momentum of the ICM introduced by the merger to dissipate quickly into other directions. As a result, the distribution of the ICM tends to be isotropic, giving the ICM a roundish morphology with small centroid offset and asymmetry. However, collisions between member galaxies are rare, so the relaxation timescale of member galaxies is larger than that of the ICM. Such cases have been simulated by Poole et al. (2006). For two clusters with a mass ratio of 1:1, the relaxation timescale for the whole system is about $t_{\text{relax}} \sim 4.4 - 5.4$ Gyr. The gaseous component generally reaches the virialization state about ~ 0.5 Gyr earlier than the dark matter. For the 10:1 mergers, the virialization timescale of the gaseous components is about 6.4 – 7.4 Gyr, while the dark matter needs much longer time ($t > 14$ Gyr) to reach the virialization criteria in r_{200} .

In Fig. 5, we explore if the difference of dynamic features between member galaxies and the ICM is related to other properties of clusters, i.e., the concentration index c (upper panels) and the cluster mass M_{500} (lower panels). The significance of the Spearman rank-order correlation p_s (see definition in p. 640 of Press et al. 1992) is used to assess weak but intrinsic correlations, with a zero value for a robust correlation and a non-zero value for no correlations. All four panels show a clear non-zero p_s , which indicates that the difference in dynamical features for member galaxies and the ICM is independent of cluster mass and concentration index.

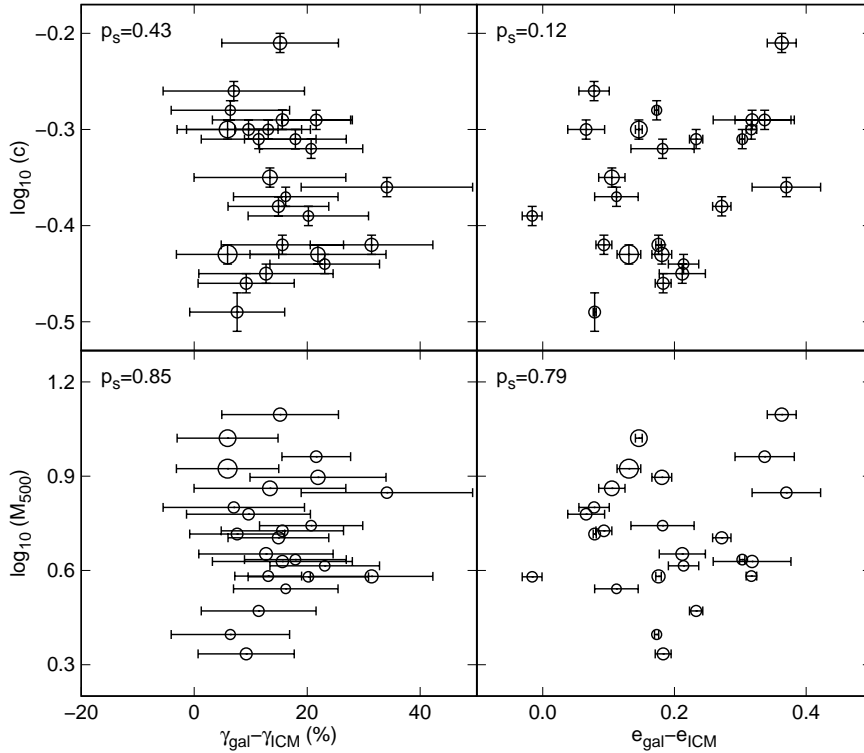


Figure 5. Left-hand panels: relations between the $\gamma_{\text{gal}} - \gamma_{\text{ICM}}$, the difference of sphere index measured from distributions of member galaxies and the ICM, against the concentration index c (upper panel) and the cluster mass M_{500} (lower panel). The circle size is proportional to $\sqrt{N_{\text{sat}}}$. The errorbars of each point are the Poisson errors. The significance of Spearman rank-order correlation p_s is written on the top-left corner of each panel. Right-hand panels: similar to the left-hand panels but for the ellipticity of galaxy clusters.

4 SUMMARY

Earlier studies have shown that member galaxies and the ICM in galaxy clusters may exhibit different dynamically relaxed states, especially in the early stages of a cluster merger (e.g., Bradač et al. 2008). Simulations suggest that the almost collisionless dark matter and member galaxies generally shows more elongated distribution (McDonald et al. 2022) and take longer time to reach the dynamical equilibrium state (e.g., Poole et al. 2006) than the diffuse gaseous component. In this study, we focus on 24 massive clusters that are in quasi-equilibrium state as indicated by their X-ray images. The cluster orientations and three kinds of dynamical parameters, i.e., the normalized centroid offset η , the sphere index γ and the ellipticity e , for the distributions of member galaxies and ICM are calculated through the same method in the same region. While the cluster orientations indicated by the two matter components are well aligned, the dynamical parameters derived from member galaxies are systematically larger than those obtained from the diffuse ICM. This suggests that the diffuse gaseous component reaches a more relaxed state than collisionless member galaxies after cluster mergers. We find that the difference in dynamical features between member galaxies and the ICM is not related to cluster mass and center concentration.

ACKNOWLEDGEMENTS

We thank the anonymous referee for insightful comments which helped us to improve the paper. This work is partially supported by the National Natural Science Foundation of China (No. 11988101, 12073036, 11833009), the science research grants from the China

Manned Space Project (No. CMS-CSST-2021-A01, CMS-CSST-2021-B01) and the National SKA Program of China (Grant No. 2022SKA0120103). HB obtains support from the Deutsche Forschungsgemeinschaft through the Excellence Cluster Origins and GC is supported by the Deutsches Zentrum für Luft- und Raumfahrt through project 50 OR 2204. This work is based on observations obtained with *XMM-Newton*, an ESA science mission with instruments and contributions directly funded by ESA Member States and NASA. Funding for the Sloan Digital Sky Survey IV has been provided by the Alfred P. Sloan Foundation, the U.S. Department of Energy Office of Science, and the Participating Institutions. SDSS acknowledges support and resources from the Center for High-Performance Computing at the University of Utah. The SDSS web site is www.sdss.org.

DATA AVAILABILITY

The data underlying this article will be shared on reasonable request to the first author. More optical and X-ray data on large samples of galaxy clusters can be found at the webpage: http://zmtt.bao.ac.cn/galaxy_clusters/.

REFERENCES

- Arnaud M., Pratt G. W., Piffaretti R., Böhringer H., Croston J. H., Pointecouteau E., 2010, *A&A*, **517**, A92
 Berrier J. C., Stewart K. R., Bullock J. S., Purcell C. W., Barton E. J., Wechsler R. H., 2009, *ApJ*, **690**, 1292

- Bradač M., Allen S. W., Treu T., Ebeling H., Massey R., Morris R. G., von der Linden A., Applegate D., 2008, *ApJ*, 687, 959
- Buote D. A., Canizares C. R., 1992, *ApJ*, 400, 385
- Carter D., Metcalfe N., 1980, *MNRAS*, 191, 325
- Clowe D., Schneider P., 2002, *A&A*, 395, 385
- Clowe D., Gonzalez A., Markevitch M., 2004, *ApJ*, 604, 596
- Clowe D., Bradač M., Gonzalez A. H., Markevitch M., Randall S. W., Jones C., Zaritsky D., 2006, *ApJ*, 648, L109
- Dawson W. A., et al., 2012, *ApJ*, 747, L42
- Donnarumma A., et al., 2011, *A&A*, 528, A73
- Faber S. M., Jackson R. E., 1976, *ApJ*, 204, 668
- Fabian A. C., 2012, *ARA&A*, 50, 455
- Golovich N., Dawson W. A., Wittman D., Ogorean G., van Weeren R., Bonafede A., 2016, *ApJ*, 831, 110
- Golovich N., van Weeren R. J., Dawson W. A., Jee M. J., Wittman D., 2017, *ApJ*, 838, 110
- Huang H.-J., Mandelbaum R., Freeman P. E., Chen Y.-C., Rozo E., Rykoff E., Baxter E. J., 2016, *MNRAS*, 463, 222
- Jee M. J., Hughes J. P., Menanteau F., Sifón C., Mandelbaum R., Barrientos L. F., Infante L., Ng K. Y., 2014, *ApJ*, 785, 20
- Lynden-Bell D., 1967, *MNRAS*, 136, 101
- Mann A. W., Ebeling H., 2012, *MNRAS*, 420, 2120
- Markevitch M., Gonzalez A. H., David L., Vikhlinin A., Murray S., Forman W., Jones C., Tucker W., 2002, *ApJ*, 567, L27
- Maurogordato S., et al., 2008, *A&A*, 481, 593
- McDonald W., Obreschkow D., Garratt-Smithson L., 2022, *MNRAS*, 516, 5289
- McGee S. L., Balogh M. L., Bower R. G., Font A. S., McCarthy I. G., 2009, *MNRAS*, 400, 937
- Niederste-Ostholt M., Strauss M. A., Dong F., Koester B. P., McKay T. A., 2010, *MNRAS*, 405, 2023
- Piffaretti R., Valdarnini R., 2008, *A&A*, 491, 71
- Piffaretti R., Arnaud M., Pratt G. W., Pointecouteau E., Melin J. B., 2011, *A&A*, 534, A109
- Plionis M., 2002, *ApJ*, 572, L67
- Poole G. B., Fardal M. A., Babul A., McCarthy I. G., Quinn T., Wadsley J., 2006, *MNRAS*, 373, 881
- Powell L. C., Kay S. T., Babul A., 2009, *MNRAS*, 400, 705
- Press W. H., Teukolsky S. A., Vetterling W. T., Flannery B. P., 1992, Numerical recipes in FORTRAN. The art of scientific computing
- Ramella M., et al., 2007, *A&A*, 470, 39
- Roettiger K., Burns J., Loken C., 1993, *ApJ*, 407, L53
- Roettiger K., Burns J. O., Loken C., 1996, *ApJ*, 473, 651
- Roettiger K., Loken C., Burns J. O., 1997, *ApJS*, 109, 307
- Santos J. S., Rosati P., Tozzi P., Böhringer H., Ettori S., Bignamini A., 2008, *A&A*, 483, 35
- Splinter R. J., Melott A. L., Linn A. M., Buck C., Tinker J., 1997, *ApJ*, 479, 632
- Struble M. F., Ftaclas C., 1994, *AJ*, 108, 1
- Wen Z. L., Han J. L., 2013, *MNRAS*, 436, 275
- Wen Z. L., Han J. L., 2015, *ApJ*, 807, 178
- Wen Z. L., Han J. L., Liu F. S., 2009, *ApJS*, 183, 197
- Wen Z. L., Han J. L., Liu F. S., 2012, *ApJS*, 199, 34
- Yuan Z. S., Han J. L., 2020, *MNRAS*, 497, 5485
- Yuan Z. S., Wen Z. L., 2022, *MNRAS*, 516, 3159
- Yuan Z. S., Han J. L., Wen Z. L., 2022, *MNRAS*, 513, 3013
- de Theije P. A. M., Katgert P., van Kampen E., 1995, *MNRAS*, 273, 30